Materials Today Electronics 15 (2026) 100198

Contents lists available at ScienceDirect

Materials Today Electronics

journal homepage: www.elsevier.com/locate/mtelec

Tuning magnetic and damping properties of soft ferromagnetic FeGaB thin films for high-frequency applications

Sumanta Kumar Karan [a,b,1,*], Shweta Sharma [a,1,*], Nicholas W.G. Smith [c,1], Yannick Pleimling [c], Stephen McGill [d], Brenden A. Magill [c], Shashank Priya [a], Bed Poudel [a,*], Giti A. Khodaparast [c,*]

[a] Department of Materials Science and Engineering, The Pennsylvania State University, University Park, PA, USA
[b] Centre for Clean Energy Engineering, University of Connecticut, CT, Storrs, USA
[c] Department of Physics, Virginia Tech, Blacksburg, VA, USA
[d] National High Magnetic Field Laboratory, Tallahassee, FL, USA

ARTICLE INFO

Keywords:
Sputtering
Thin film
FeGaB
Physical vapor deposition
Soft magnetic materials
Ferromagnetic resonance
Time-resolved MOKE

ABSTRACT

Soft magnetic materials are widely used in inductors, transformers, and magnetic sensors. Probing their fundamental properties is therefore crucial to gain insights into improving their static and dynamic magnetic behavior. Herein, we report results on iron-gallium-boron (FeGaB) thin films grown on Si substrate using magnetron co-sputtering. Systematic investigation was carried out to examine the influence of sputtering process parameters on tuning the structure and magnetic properties of FeGaB thin films. By precisely controlling FeGa and B targets' sputtering power, optimal $(Fe_{1-y}Ga_y)_{1-x}B_x$ films were realized that exhibit excellent magnetic softness (H_c ~ 6-11 Oe), and a remarkably low effective Gilbert damping (α_{eff} ~ 0.009-0.015). Furthermore, ultrafast magnetization dynamics characterized using time-resolved magneto-optical Kerr effect (TR-MOKE) revealed slow relaxation times of the excited magnetic state in the FeGaB thin films. Collectively, these results confirm that the developed FeGaB thin films have promising high-frequency applications including magnetic sensors.

Introduction

Soft magnetic thin films with large magnetostriction and low damping factors are in demand for high-frequency applications [1,2]. This is due to their favorable attributes including low magnetic coercivity, large permeability, high ferromagnetic resonance (FMR) frequency, and reduced eddy current losses [2–7], which benefit applications like sensors, actuators, microwave devices, and magneto-electric energy harvesters [8–10]. Particularly, a low Gilbert damping coefficient is crucial for fast switching and low loss operations in spintronic and high-frequency systems [9]. Magnetic thin films are commonly deposited using physical vapor deposition techniques such as sputtering and thermal evaporation [11,12], which allow precise control over film thickness, composition, and microstructure.

Galfenol, an iron-gallium alloy ($Fe_{1-x}Ga_x$; $12<x<25$), exhibits prominent properties including a large magnetostriction (≤275 ppm), high saturation magnetization (≤18 kG), moderate saturation field (~ 100 Oe), and high magneto-mechanical coupling factor (~0.4) [13,14]. These properties render FeGa thin films suitable for strain-coupled magnetoelectric devices, where the magnetostrictive FeGa layer induces a change in the size/shape of the piezoelectric layer, thereby generating electricity in response to an applied magnetic field [10,11,15,16]. However, despite these advantages, FeGa films also exhibit sub-optimal soft magnetic behavior due to their relatively high electrical conductivity, high stress, and large damping factor, hindering their performance in high frequency applications [10,17]. Addition of Ni, N, and C into FeGa to form FeGaNi, FeGaN, FeGaC alloys has been demonstrated as a way to enhance its magnetostrictive behavior [18–20]. In contrast, incorporating B into FeGa to form FeGaB alloy has been shown to refine the grain size and reduce magnetocrystalline

* Corresponding authors.
E-mail addresses: sumanta.karan@uconn.edu, sumanta.karan.fula@gmail.com (S.K. Karan), sbs6772@psu.edu (S. Sharma), bup346@psu.edu (B. Poudel), khoda@vt.edu (G.A. Khodaparast).
[1] These authors contributed equally.

https://doi.org/10.1016/j.mtelec.2026.100198
Received 13 August 2025; Received in revised form 6 January 2026; Accepted 22 January 2026
Available online 30 January 2026

anisotropy, resulting in excellent soft magnetic behavior and microwave properties [4,13,21–24]. The FeGaB thin films are characterized by low coercivity, reduced energy loss during magnetization reversal, high sensitivity to weak magnetic fields, low damping, high magnetic permeability and thermal stability [7]. These properties make FeGaB thin films relevant for a wide range of spintronic devices, magnetic sensors, and high frequency integrated inductors and transformers for power electronics [7,16,25,26].

Several studies have investigated FeGaB thin films for high-frequency applications. Cao *et al.* conducted comparative analysis of the magnetic properties of FeGa, FeGaN, and FeGaB films at high frequency [10]. It was found that FeGaB films showed the best results in terms of soft magnetic nature with a self-biased (~ at zero external bias field) FMR frequency of 1.83 GHz and a low damping factor of 0.023. Yadagiri *et al.* obtained damping parameters of 0.0071 and 0.0087 through FMR measurement on FeGaB and Al_2O_3/FeGaB multilayered thin films patterned on Si substrates, respectively [22,27,28]. Li *et al.* developed a highly sensitive (~2.8 Hz/nT) AlN/FeGaB resonator-based magnetic field sensor for DC/low frequency range [29]. Liu *et al.* demonstrated the electric field strain-induced change in ferromagnetic resonance of FeGaB/PZN-PT (011) magnetoelectric composites [30]. Lou *et al.* examined the impact of B addition on the soft magnetism, magnetostriction, and microwave properties of FeGaB thin films [7]. These prior reports, however, provide a limited discussion on the film growth process and the effect of deposition parameters on properties of FeGaB thin films. Further, in these prior studies, there is a lack of visible optics for investigating the magneto-optical response as well as understanding the ultrafast magnetization dynamics of FeGaB thin films.

Controlling magnetization dynamics on femtosecond timescales is fundamentally important for integrated opto-spintronic devices [31]. Understanding the dynamic process of how a magnetic material returns to equilibrium after excitation by intense laser pulses, together with its ferromagnetic resonance (FMR) response, provides important criteria for achieving ultrafast spin control. The direct excitation of spin populations through laser pulses has been studied extensively in semiconductors where spin-polarized electrons in the conduction band can be generated by circularly polarized light because of the dipole-allowed optical selection rules [32]. In the presence of a net magnetic moment (*i.e.,* in a ferromagnetic semiconductor) [33,34], spin-transfer torque between spin-polarized electrons and the magnetization in the semiconductor can occur. It has been shown by Stanciu *et al.* [35] that circular polarization of light in the absence of a magnetic field can switch the magnetization of a metallic ferrimagnet, and this observation has launched the field of all-optical helicity-dependent switching (AO-HDS) in ferrimagnets. This effect was later also reported in ferromagnets; however, in most cases, AO-HDS in ferromagnetic metals requires many laser pulses to fully switch their magnetic states [36–38]. Recent magnetization-dynamics studies on FeGaB have mainly focused on heterostructures, where interfacial coupling shapes the response, including FeGaB/PMN-PT magnetoelectric heterostructure for electric-field tuning [39], and FeGaB-BiSb interfaces for light- and microwave-driven spin pumping [40]. To the best of our knowledge, intrinsic ultrafast demagnetization has only recently been reported in FeGa films using time-resolved pump-probe method [41]; however, boron incorporation in FeGa can modify the microstructure and relaxation pathways. This motivates a study of magnetization relaxation dynamics post ultrafast demagnetization.

Building upon the prior studies, here, we systematically investigate the influence of sputtering process parameters on the structure and magnetic properties of FeGaB films. Changes in FeGa and B target power, substrate temperature, and sputtering time affect the amount of B doping in FeGa film, influencing its characteristics. Under optimal sputter power conditions (i.e., FeGa: 60 W and B: 40 W), the FeGaB thin film exhibits low coercivity, narrow FMR linewidth, and low effective Gilbert damping. Specifically, when grown at room temperature (RT), the optimal FeGaB thin film shows relatively high magnetization (M_s ~ 1790 emu/cc or $4\pi M_s$ ~ 22.5 kGauss), low coercivity (H_c ~ 36 Oe) and low Gilbert damping constant (~0.015). At growth temperature of 200 °C, the optimal FeGaB thin film shows moderate magnetization (M_s ~770 emu/cc or $4\pi M_s$ = 9.7 kGauss), ultra-low coercivity (H_c ~ 6 Oe) and an even lower damping constant (~0.009). Further, ultrafast magnetization dynamics in the optimal FeGaB films were explored via time-resolved magneto-optical Kerr effect (TR-MOKE), a powerful tool to study laser-induced magnetization changes in a ferromagnetic material [24]. Additionally, we also demonstrate that the magneto-optical response of FeGaB films can be effectively probed using magnetic circular dichroism (MCD) under visible optical excitation (see Supporting Information, Note S2 and Figure S3, S4). These findings reveal new dynamical responses in FeGaB which can offer pathways for further material exploration and application.

Methods and characterization

The FeGaB thin films were deposited on silicon (100) substrates using high purity 2-inch diameter $Fe_{80}Ga_{20}$ and B targets via magnetron co-sputtering (Make: Kert J. Lesker; Model: PVD 75 PRO LINE). The vacuum chamber was evacuated to a base pressure of 1×10^{-7} Torr, with a constant Ar pressure maintained at 8 mTorr during deposition. Sputtering powers in the range of 20 to 60 W, corresponding to power densities of approximately 1.0 to 3.0 W/cm^2, were applied to the FeGa and B targets to optimize the film's stoichiometry and magnetic properties, while maintaining stable plasma conditions. In particular, the B target power was limited to 50 W, as higher powers resulted in target overheating and unstable deposition. Conversely, target powers below 20 W were insufficient to reliably ignite and sustain the plasma. The crystallographic characteristics of FeGaB thin films were assessed using X-ray diffraction (XRD) through a PANalytical X'Pert X-ray diffractometer with a Cu Kα source (λ=1.544 Å) in the θ-2θ mode. The thickness of the films was measured using a surface profilometer and were found to be in the range of 40 nm to 75 nm depending on sputter parameters. To investigate the surface morphology of the FeGaB thin films, field emission scanning electron microscopy (FESEM) was employed. Elemental composition was determined through Energy Dispersive X-ray (EDAX) analysis and X-ray photoelectron spectroscopy (XPS). Ion sputtering was done using 2 kV Ar^+ rastered over a 2 mm × 2 mm area to get the exact elemental analysis in XPS. Static magnetic properties of the FeGaB films in-plane geometry were measured by a vibrating sample magnetometer using Lakeshore 8600 Series in the range of +6000 to -6000 Oe DC magnetic field at room temperature.

Ferromagnetic Resonance (FMR)

FMR was used to measure the dynamic magnetic properties of the FeGaB thin films. To probe FMR, each sample was excited with a fixed microwave frequency from a coplanar waveguide, while a quasistatic magnetic field was applied in the film plane. By employing a 700 Hz modulation field, collinear with the quasi-static field, the resonance signal was acquired with a lock-in amplifier connected to a microwave diode. Hence, the measured resonance spectrum was the derivative of the microwave absorption with respect to the quasi-static field.

Time-Resolved Magneto-Optical Kerr Effect (TR-MOKE)

TR-MOKE was employed on the optimized FeGaB thin films to understand ultrafast magnetization dynamics. Using a two-color pump/probe (400 nm/800 nm), TR-MOKE response of one of the samples (*D1*) was monitored. In this process, the laser source was an amplified Ti: Sapphire oscillator with a repetition rate of 1 kHz, with a wavelength of 800 nm and a pulse duration of ~ 100 fs and ~1 W output power. 90% of the oscillator's output power was used to frequency double to 400 nm using a 0.5 mm thick BBO crystal and generated 1 mW of power with an estimated fluence of 4 mJ cm^{-2}. The pump pulses were modulated by a

chopper at 211 Hz. The probe pulses at 800 nm were attenuated to ~10 μW, corresponding to a fluence of 40 μJ cm^{-2}. The 400 nm pump pulses were circularly polarized, and the reflected 800 nm probe pulses from the sample were directed through a Wollaston prism to separate the S and P polarizations. Balanced Si-photodiode detection was used to measure the differences between the S and P polarizations as a function of the time delay between the pump and probe pulses. Figs. 1 (b) shows the schematic of the TR-MOKE set-up.

RESULTS AND DISCUSSION

Structural analysis

Figs. 2 (a-d) show the normalized log scale X-Ray diffraction (XRD) patterns of the FeGaB thin films synthesized under varying sputtering power at RT for 30 minutes. Figs. 2 (a) shows the XRD spectra of FeGaB films (samples *A1, B1, C1*, and *D1*) prepared by varying the DC sputtering power of the FeGa target while maintaining the B target at fixed 40 W RF power. Samples *B1, C1*, and *D1* exhibit a (110) bcc diffraction peak that becomes increasingly pronounced as FeGa target power increases. In contrast, the (110) peak is nearly absent in sample *A1*, indicating reduced crystallinity and increased amorphization under low FeGa power (~30 W) condition. Si substrate peaks are observed around 2θ~33° and 2θ~70°. Fig. 2 (b) shows the zoomed-in view of Fig. 2 (a), revealing a shift in the (110) diffraction peak towards higher angles *i.e.,* from $2\theta \sim 44.22°$ to $2\theta \sim 44.42°$ as FeGa power increases from 30 W to 60 W, indicating lattice contraction.

Figs. 2 (c) shows the XRD patterns of the FeGaB films developed under varying B power while maintaining FeGa power fixed at 30 W (samples *F1, A1,* and *G1),* and at 60 W (samples *D1* and *E1*). The zoomed-in view in Figs. 2 (d) shows no significant (110) peak at 30 W FeGa power regardless of B power (samples *F1, A1, G1*). This suggests an amorphous structure due to insufficient FeGa content, implying B power has little influence on crystallinity under low FeGa power conditions. However, at 60 W FeGa power, the (110) diffraction peak appears and broadens with an increase in B power from 30 W to 40 W (samples *E1* and *D1*). In addition, the (110) peak shifts towards lower angles, *i.e.,* from 2θ~44.42° to 2θ~44.39° with an increase in B power from 30 W to 40 W, indicating lattice expansion due to B atoms occupying interstitial sites in FeGa. The broadening (or FWHM increase) of the (110) peak with increasing B power indicates higher B doping resulting in an amorphous nature and a decrease in grain size of FeGaB films from 15 nm to 13 nm (*D1* and *E1*, Table 1). The results are similar to those earlier reported by Lou *et al.* [7].

Table 1 summarizes the 2θ, FWHM, and calculated grain size corresponding to the (110) diffraction peak of the FeGaB thin films deposited under varying sputtering conditions. The average grain size (D) was calculated using Debye-Scherrer's formula, $D = K\lambda/\beta cos\theta$ [42], where K indicates the shape factor, λ indicates the wavelength of Cu-Kα radiation, and β indicates the FWHM. In our analysis, we employed a value of K=0.94, which is appropriate for spherical crystallites with cubic symmetry, a reasonable assumption for sputtered FeGaB thin films [43–45]. It is to be noted that the FeGaB films prepared under low FeGa power of 30 W and varying B power (30 W, 40 W, and 50 W), i.e., samples *F1, A1,* and *G1*, lack a detectable (110) diffraction peak, so their FWHM and grain size could not be calculated, and hence are not listed in Table 1.

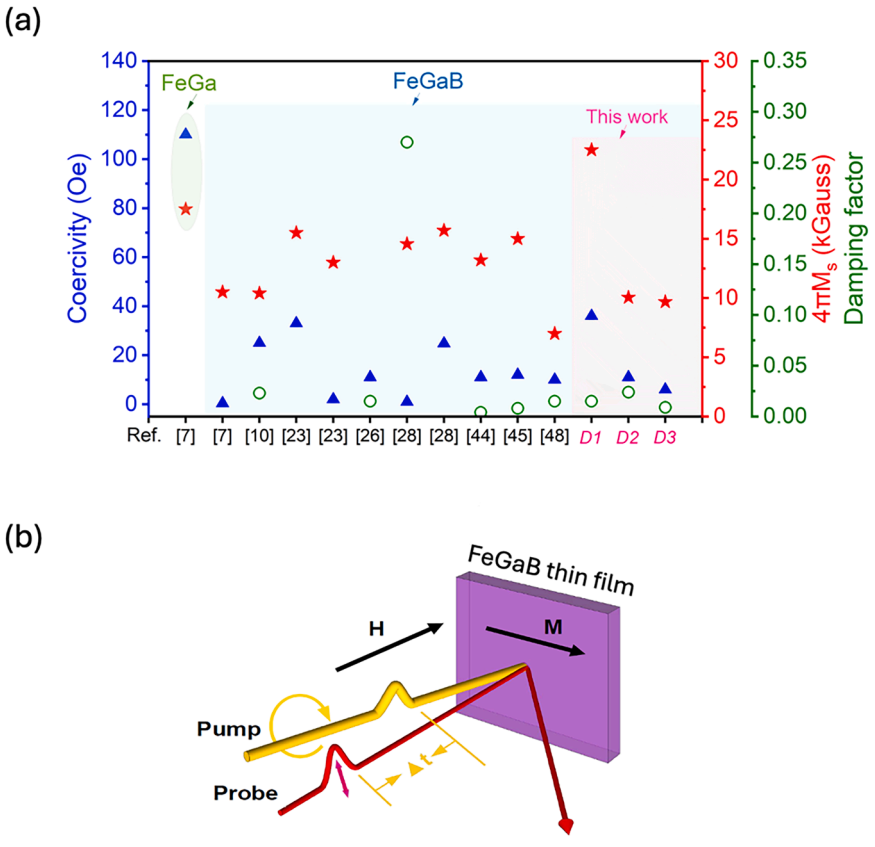

Figs. 1. (a) Comparison of our measured values of coercivity and saturation magnetization with those reported in the literature for FeGaB thin films. (Note: The x-axis in panel (a) corresponds to reference numbers cited in the main manuscript; D1-D3 represent the configurations from this work). (b) The geometry of our measurements with respect to the applied field (H) and pump/probe pulses. The pump and probe beams had a 5-degree angle separation. The measurements were performed inside an Oxford split coil magnet with optical windows. For TR-MOKE, the pump at 400 nm was circularly polarized and the 800 nm probe was linearly polarized. The magnetization easy axis (M) of the FeGaB thin film (sample D1) was in the sample plane.

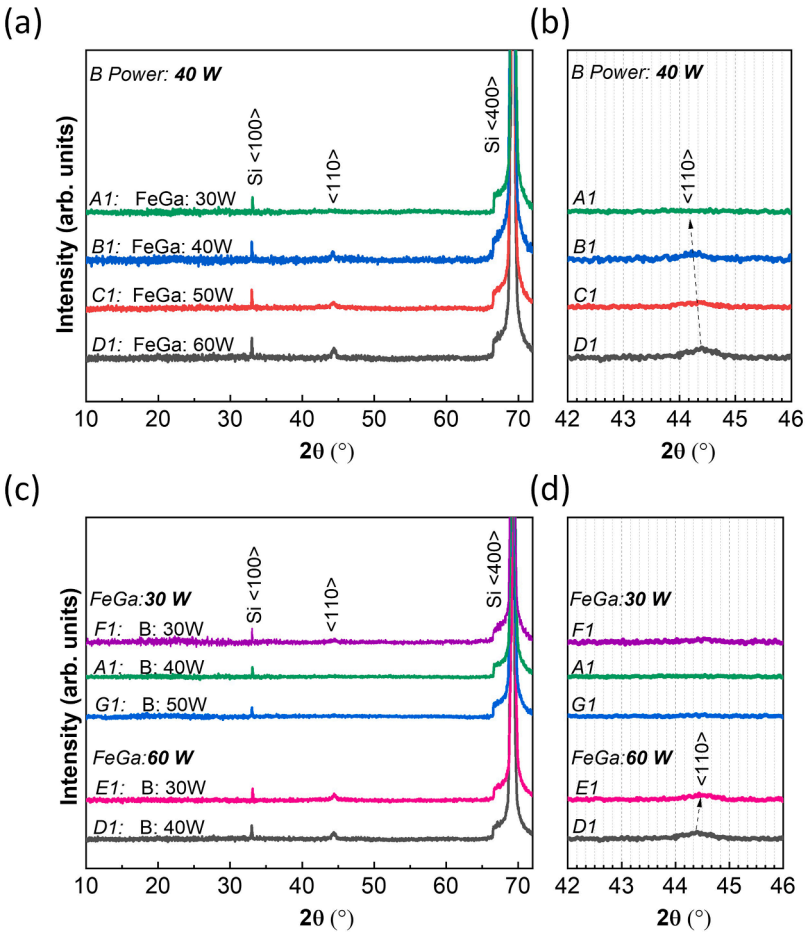

Figs. 2. Normalized X-Ray diffraction pattern of FeGaB thin films deposited by varying sputtering power of (a) iron gallium (FeGa) target, (c) boron (B) target. Figs. 2 (b) and 2(d) are zoomed-in views showing shifts in peak position with respect to target power variation.

Table 1
2θ, full width at half maximum (FWHM), and calculated grain size for (110) peak of FeGaB thin films prepared under varied FeGa and B sputtering power conditions. (Here '-' implies the parameter could not be estimated from the corresponding XRD pattern due to the absence of (110) peak).

Sample ID	Sputter Power (FeGa _B) (in Watts)	Deposition time (minutes)	Deposition temperature ($^{\circ}C$)	Peak Position, 2θ ($^{\circ}$)	FWHM, β ($^{\circ}$)	Grain size, D (nm)
A1	(30_40)	30	RT	44.22	-	-
B1	(40_40)	30	RT	44.26	0.43	20.84
C1	(50_40)	30	RT	44.30	0.62	14.46
D1	(60_40)	30	RT	44.42	0.66	13.59
E1	(60_30)	30	RT	44.50	0.59	15.20
F1	(30_30)	30	RT	-	-	-
G1	(30_50)	30	RT	-	-	-

Magnetic hysteresis measurements

Table 2 summarizes the coercive field (H_c) of all the FeGaB samples along with their deposition parameters. Figs. 3 (a,b) depict the normalized change in magnetic hysteresis (M/M_s) of samples *A1-G1* with varying sputtering power of FeGa and B targets, respectively. The deposition time (~ 30 minutes) and temperature (~ RT) were kept constant for the above samples. The films grown under a high FeGa power of 60 W (samples *D1* and *E1*) achieve magnetic saturation (M_s) at lower in-plane applied fields. The inset of Figs. 3 (a,b) show the variation of H_c with FeGa and B target power, respectively, highlighting the crucial role of sputtering power in influencing the magnetic coercivity of the sample. Comparing samples *D1* and *E1* (inset of Figs. 3 (a)) suggests that with an increase in B power from 30 W to 40 W, H_c decreases from 42 Oe to 36 Oe, at fixed FeGa power (~60 W). The lower H_c indicates higher B doping and hence enhanced magnetic softness. It can be

Table 2
Coercivity values (H_c (Oe)), of different FeGaB thin films prepared under varied sputtering conditions.

Sample ID	Sputter Power (*FeGa _B*) (Watts)	Deposition time (minutes)	Substrate temperature ($^{\circ}C$)	Coercivity, H_c (Oe)
A1	(30_40)	30	RT	40
B1	(40_40)	30	RT	42
C1	(50_40)	30	RT	54
D1	(60_40)	30	RT	36
E1	(60_30)	30	RT	42
F1	(30_30)	30	RT	44
G1	(30_50)	30	RT	38
D2	(60_40)	60	RT	11
D3	(60_40)	60	200	6

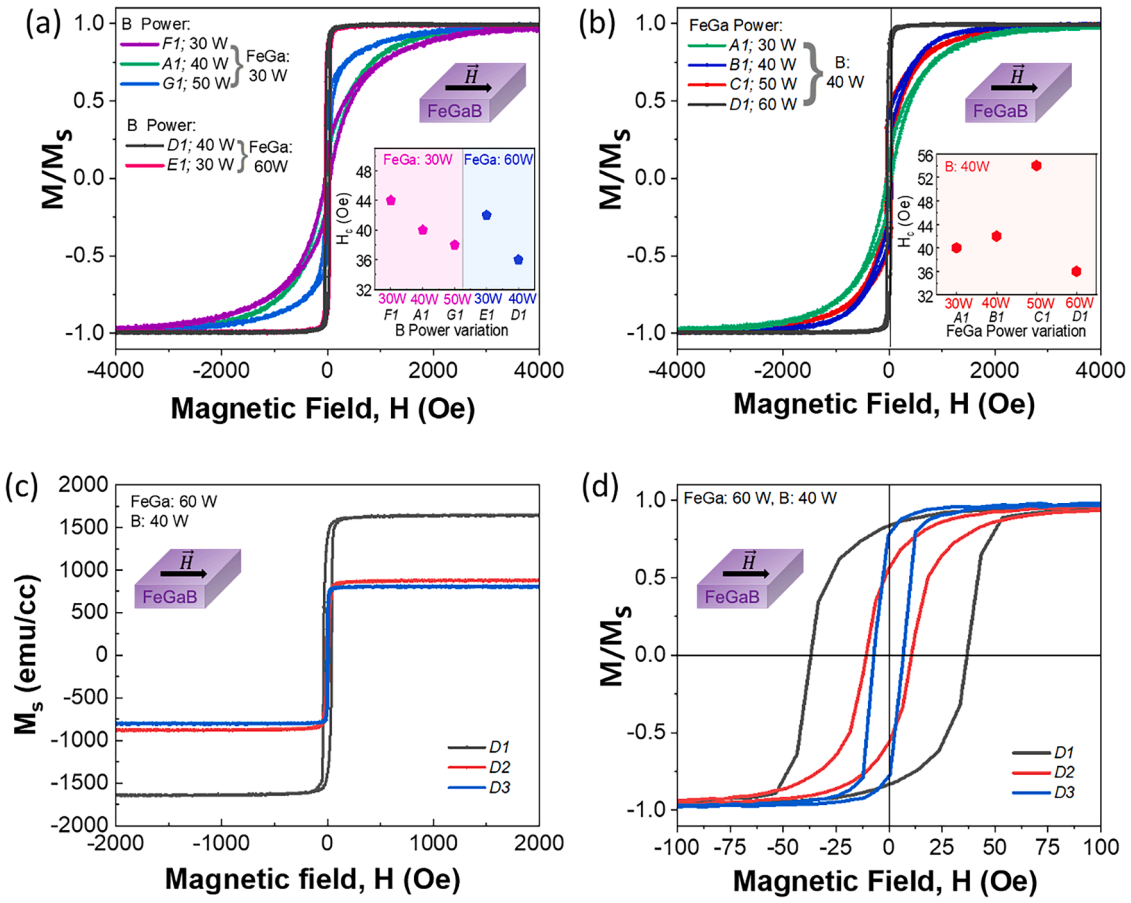

Fig. 3. Normalized (M/M_s) magnetic hysteresis of FeGaB thin films deposited by varying sputtering power of (a) boron (B) target, (b) iron gallium (FeGa) target, under identical deposition time (~ 30 minutes) and temperature (~RT) conditions. Magnetic field dependence of (c) saturation magnetization, and (d) normalized (M/M_s) magnetic hysteresis of FeGaB thin films prepared under optimal targets' power (FeGa: 60 W, B: 40 W) but different deposition time and temperature.

concluded that amongst all the samples grown for 30 minutes at RT (*A1-G1*), sample *D1* deposited at 60 W FeGa power and 40 W B power, exhibits a relatively lower H_c ~36 Oe, implying higher magnetic softness.

Once the favorable sputter power conditions (i.e., FeGa/B: 60W/40 W) were identified for attaining a soft magnetic FeGaB film (sample *D1*), the influence of deposition time (sample *D2*) and substrate temperature (sample *D3*) were studied (Table 2 and Figs. 3 (c,d)). The samples *D2,* and *D3* were prepared under optimal 60 W FeGa power and 40 W B power conditions. A substrate temperature of 200°C was selected for sample *D3* based on literature reports indicating reduced coercivity (H_c) and improved soft magnetic behavior at elevated growth temperatures [24,27,42]. Figs. 3 (c,d) show sample *D2* exhibits lower coercivity, H_c ~11 Oe and moderate saturation magnetization, M_s ~ 800 emu/cc (or $4\pi M_s = 10.1$ kGauss) compared to sample *D1* with higher H_c ~ 36 Oe and M_s ~ 1790 emu/cc (or $4\pi M_s$ ~ 22.5 kGauss). Furthermore, sample *D3* exhibits the lowest H_c ~ 6 Oe and M_s ~ 770 emu/cc (or $4\pi M_s = 9.7$ kGauss), indicating enhanced magnetic softness at the expense of M_s, likely due to higher B content. These samples were further studied for morphological, elemental composition analysis, and dynamic magnetic properties.

Morphological and elemental analysis

To understand the microstructure of the optimal samples *D2* and *D3*, FESEM technique was utilized to analyze the surface morphology, particle size, and thickness of the thin films. A comparative analysis of the morphology of FeGaB films with a reference FeGa thin film sample was conducted to understand the impact of B doping on microstructure. All the microstructure images presented in Figs. 4 (a-c) show uniformly distributed fine grains with no cracks. Figs. 4 (a,d) provide a top-view and cross-sectional view of the reference FeGa thin film grown under identical parameters.

The surface microstructure presents rice-like granular appearance with crystalline nature and the hard magnetic characteristic of the FeGa thin film (Fig. 4 (a)) [46,47]. Figs. 4 (b,e) depict the top-view and cross-sectional view of sample *D2*. As B is incorporated into FeGa, the surface morphology becomes smooth and grain size reduces, indicating a rise of amorphous nature of the FeGaB thin film (Fig. 4 (b)), and it can be supported from the lower coercivity of the FeGaB thin films. Figs. 4 (c,f) show the top-view and cross-sectional view of sample *D3*. It can be inferred from these images that with substrate temperature of 200°C (*D3*), the FeGaB grain size only minimally increases while the overall morphology remains the same as sample *D2, i.e.*, a densely packed distribution of fine grains. The interstitial boron disrupts the lattice of FeGa, reducing the grain size of the films, and leading to reduced magnetocrystalline anisotropy and softer magnetic properties [1]. The measured grain size in FeGa thin film is ~40±2 nm (Fig. 4 (a)) whereas for the FeGaB thin film (sample *D2*), it is ~10±2 nm (Fig. 4 (b)). The lower grain size suggests softer magnetic properties of FeGaB thin film grown at 60/40 W power for 60 minutes (sample *D2*; Fig. 4 (b)). The elevated substrate temperature of 200°C during growth leads to the formation of finer grains with a slight increase in grain size to ~18±2 nm (sample *D3*; Fig. 4 (c)), due to possible weak surface atomic diffusion [46].

The measured thickness of the reference FeGa thin film grown at RT for 60 minutes is ~221 nm. While for FeGaB thin films grown at RT for 30 minutes (*D1*) and 60 minutes (*D2*), the thicknesses are ~32 nm and ~70 nm, respectively. This suggests that addition of B element in FeGa

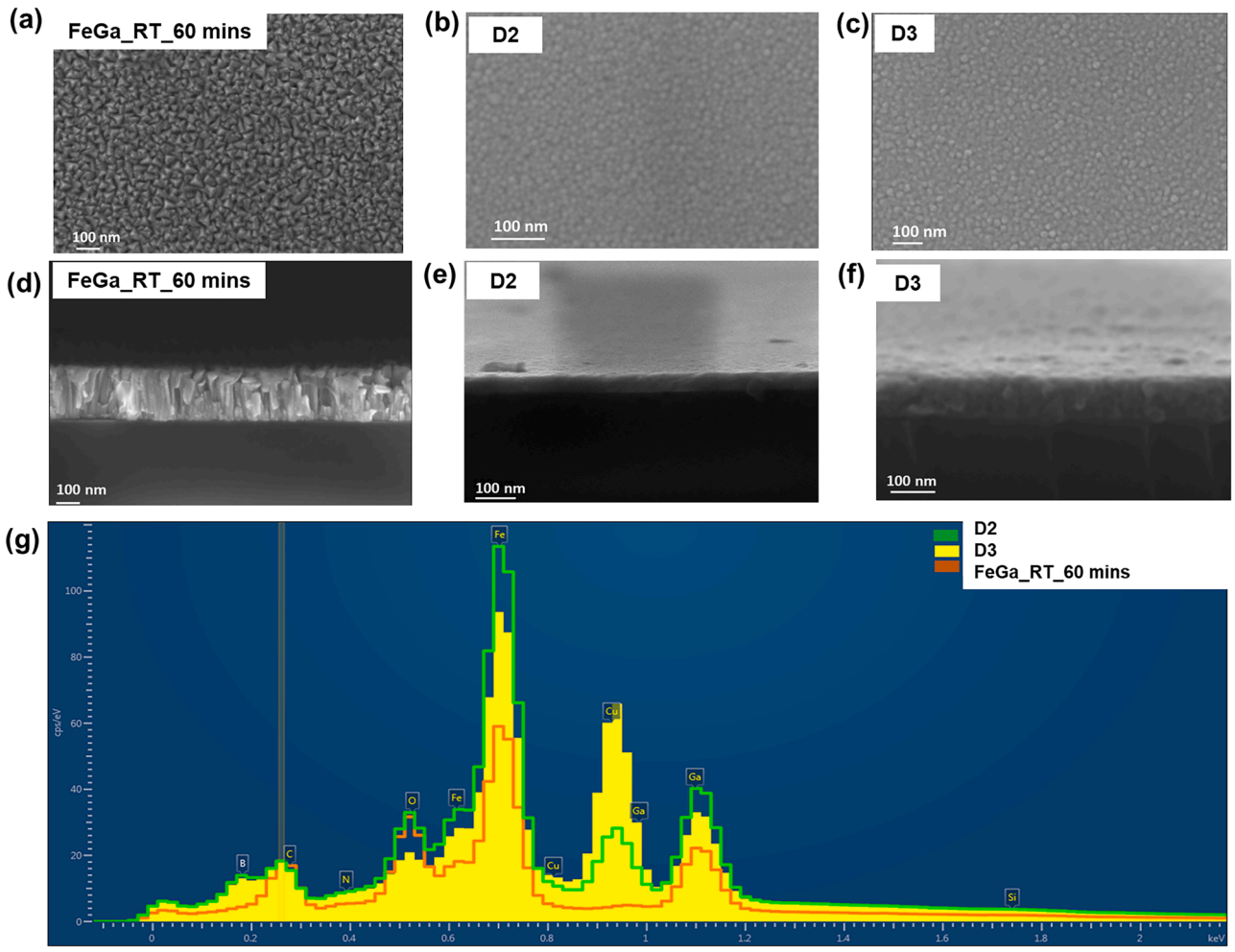

Fig. 4. (a-f) The microstructure of reference FeGa film and as-prepared D2 and D3 FeGaB films in the top view (a-c), and cross-sectional (d-f) view, respectively. (g) EDAX analysis of FeGa, D2 and D3 FeGaB thin films under FESEM study.

alloy reduces the rate of deposition by a factor of ~3.1 at RT. Further, increasing the substrate temperature (~200°C) reduces the deposition rate ~ 3.7 times, as evidenced by the reduced thickness (~59 nm) of the FeGaB sample *D3* grown for 60 minutes, compared to the reference FeGa film (Figs. 4 (d–f) and Figure S1). Even the deposition rate of the FeGaB alloy grown under the same target power with a temperature of 200°C is observed to decrease by ~1.1 times compared to the deposition rate of the FeGaB alloy grown at RT, as shown in Figure S1. EDAX analysis in Fig. 4 (g) confirms the presence of boron (B) in the FeGaB thin films prepared at room temperature and 200 °C (samples *D2* and *D3*, respectively). The reference FeGa sample showed no B peak, while clear B peaks were observed in the FeGaB films. We have estimated the composition from the EDAX to understand the deviation from the desired composition. The evaluated estimate of the compositions is as follows: FeGa reference: $Fe_{78}Ga_{22}$, *D2*: $Fe_{66}Ga_{20}B_{14}$, *D3*: $Fe_{69}Ga_{16}B_{15}$. This composition indicates that Ga content deviates from the nominal value, especially in *D3*, but still remains within the expected variation range typical for co-sputtered multi-element thin films. However, we were unable to reliably quantify the surface composition of B, which may be attributed to one or both of the following factors: (i) surface oxidation resulting from ambient exposure, and (ii) the close atomic energy levels of B and C, potentially leading to signal overlap or misidentification during EDAX. Therefore, to further investigate the elemental composition and chemical bonding states, X-ray photoelectron spectroscopy (XPS) was employed on the *D2* and *D3* FeGaB samples (Fig. 5 and Figures S2(a-f)).

The XPS surface survey scan spectra of the FeGaB films reveal the possible presence of organic ingredients (CH_x, C-O and O-C=O) as well as mixtures of oxides of B, Ga, and Fe, and small amounts of reduced Fe, Ga, and B as shown in Fig. 5 (a), Note S1, Figure S2 (supporting information). The unwanted C peak may arise from the carbon contaminants adsorbed on the surface of investigated samples, while O elements may arise from the surface oxidation of the thin films when kept for a considerable long time in the open air. Hence, to get the accurate composition of the elements in the FeGaB thin films, the sub-surface was exposed by ion sputtering, and individual elements were scanned as shown in Figs. 5 (b-d). The XPS technique revealed the binding energy of elements Fe, Ga, and B in samples *D2* and *D3*, where the satellite peak of each element was deconvoluted using the XPS software to obtain their binding energies. The determined binding energies of Fe $2p_{3/2}$, Ga $2p_{3/2}$, and B 1 s are 707, 1116, and 191.5 eV, respectively, which are well-matched with the standard values of these elements [10,48,49]. The ion sputtered surface confirms that the B element is doped into FeGa films, and the elemental composition of these alloys is estimated to be approximately $Fe_{67}Ga_{16}B_{17}$ (*D2*) and $Fe_{68}Ga_{12}B_{20}$ (*D3*) by fitting the spectra area of each peak of Fe $2p_{3/2}$, Ga $2p_{3/2}$, and B 1 s in XPS characteristic graphs. The higher B content observed in sample *D3* is consistent with its lower H_c when compared with sample D2 (see Table 2). The observed deviation from the intended $Fe_{80}Ga_{20}$ composition is attributed to several factors inherent in co-sputtering processes, particularly in multi-target systems involving a third light element (Boron). These include differential sputtering yields, preferential

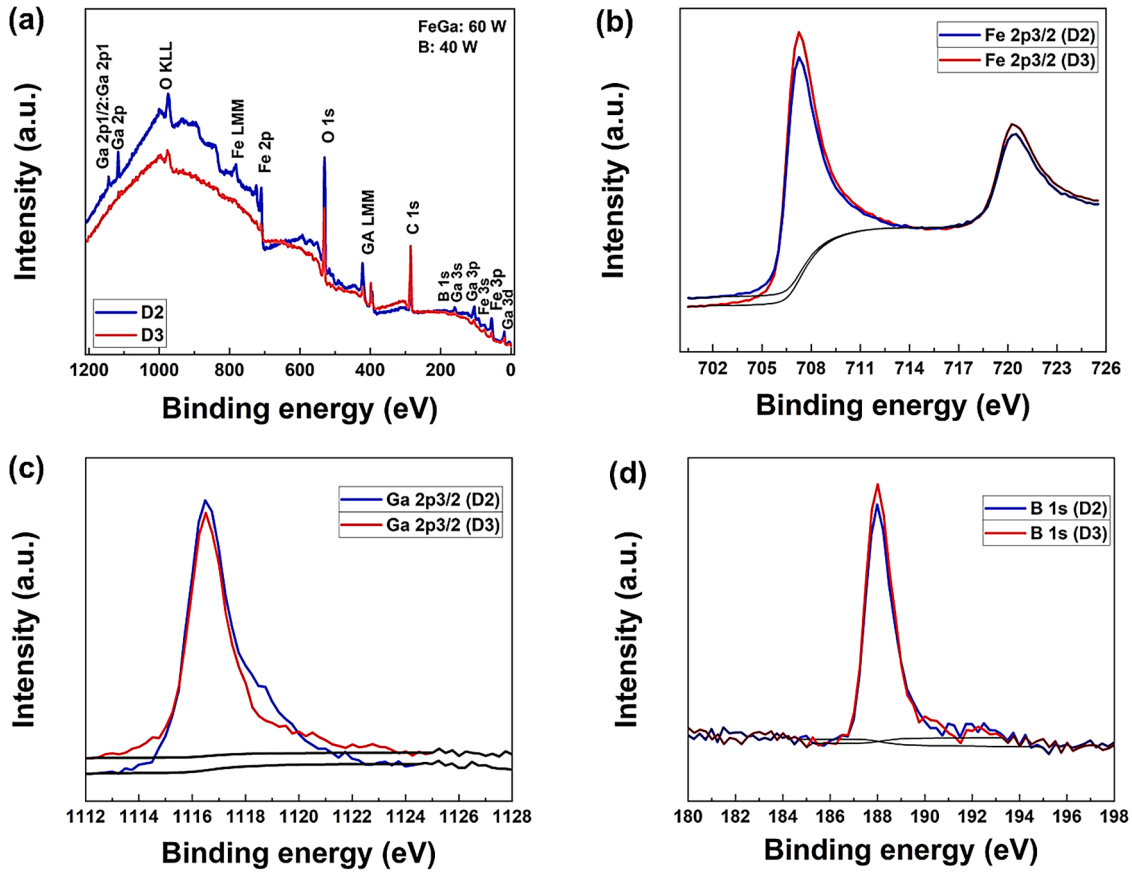

Fig. 5. (a) XPS survey spectra (without ion sputter techniques) of FeGaB thin film grown at RT (D2) and 200°C (D3) under 60/40 W power for 60 minutes. (b-d) XPS deconvoluted spectra (ion sputter technique used) for D2 and D3 FeGaB thin film samples.

re-sputtering of Ga atoms due to their lower atomic mass, local plasma density variations, and B-induced changes in the film growth kinetics and phase formation [7,50]. In comparison to the RT grown thin film (*D2*), the film prepared at higher deposition temperature (*D3*) shows more B content and a lower Ga/Fe ratio, although the FeGa target composition is the same as $Fe_{80}Ga_{20}$.

Ferromagnetic Resonance

To examine magnetization dynamics in the optimal FeGaB thin film

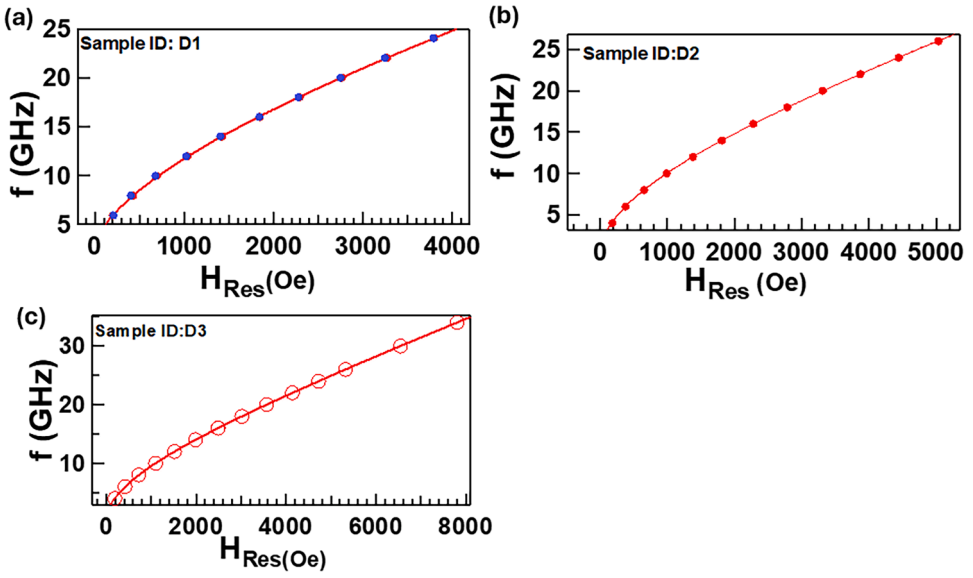

Fig. 6. Dispersion Relationships as derived from FMR frequency vs resonance peak for three samples, (a) D1, (b) D2, and (c) D3. The dispersion relationships were then fit with the Kittel model assuming no in-plane magnetocrystalline anisotropy. For sample D1 (panel a) we tested two in-plane field directions rotated 90 degrees with respect to each other. Note there is little difference between each angle (blue and red points) in D1; therefore, the Kittel fit for each rotated direction is nearly identical. (For interpretation of the references to colour in this figure legend, the reader is referred to the web version of this article.)

samples, broadband ferromagnetic resonance (FMR) measurements were performed. FMR is a common method for probing the magnetic states when the system is excited out of equilibrium to extract important magnetic properties, such as damping and magnetic inhomogeneity. The origin of the dissipation in excited ferromagnetic systems is of fundamental interest for understanding the magnetization dynamics. Controlling magnetic damping could also be important for reducing the switching current and increasing the speed of magnetic memory devices. For the FMR measurements, three optimal FeGaB thin film samples were considered – namely, samples *D1, D2*, and *D3*; their deposition parameters and properties are described in Tables 1 and 2.

First, we examine the associated dispersion relationships extracted from FMR for samples *D1, D2*, and *D3*, which are shown in Figs. 6 (a-c). We utilize the Kittel model for a thin film with magnetocrystalline anisotropy to extract both the g-factor of each sample and the effective magnetization as indicated in Eq. 1 [51].

$$f = \frac{2\pi g \mu_b}{h} \sqrt{\left[(H + H_{ani})\left(H + H_{ani} + 4\pi M_{eff}\right)\right]} \quad (1)$$

We fit Eq. 1 to the dispersion relationships shown in Fig. 6 where we assume that the in-plane magnetocrystalline anisotropy field is very small and so we set $H_{ani} = 0$ Oe. This low anisotropy field is supported by Fig. 6 (a), sample *D1*, where it is shown that the dispersion relationship is nearly identical for both an in-plane magnetic field set at 0 degrees relative to the (001) crystal axis and 90 degrees relative to the crystal axis. The in-plane crystalline anisotropy field for FeGaB has previously been shown to be less than 100 Oe, dropping with increasing B content [7]. In samples *D2* and *D3*, there is relatively more B content than *D1* which reduces crystallinity so it may be assumed that their associated in-plane magnetocrystalline anisotropy is also very small. The associated g-factors and M_{eff} for samples *D1, D2*, and *D3* are g = 2, 2.05, 2.11 and M_{eff} = 1274.5 ± 400 emu/cc, 892.5 ± 19.1 emu/cc, and 762 ± 2 emu/cc. These g-factors are close to values reported recently for FeGaB films of B content of about 9% [52]. The saturation magnetization as given by VSM (Fig. 3) for samples D2 (M_{Sat} = 800 emu/cc) and D3 (M_{Sat} = 770 emu/cc) are relatively close to the calculated FMR effective magnetization with differences potentially attributable to low perpendicular surface anisotropy. However, there is a larger difference in the saturation magnetization (M_{Sat} = 1770 emu/cc) of sample *D1* and its calculated M_{eff}. This difference could be due to the assumption that in-plane crystalline anisotropy is 0 Oe in the low B content *D1* sample is incorrect, which is supported by the large error in the M_{eff}. If we assume

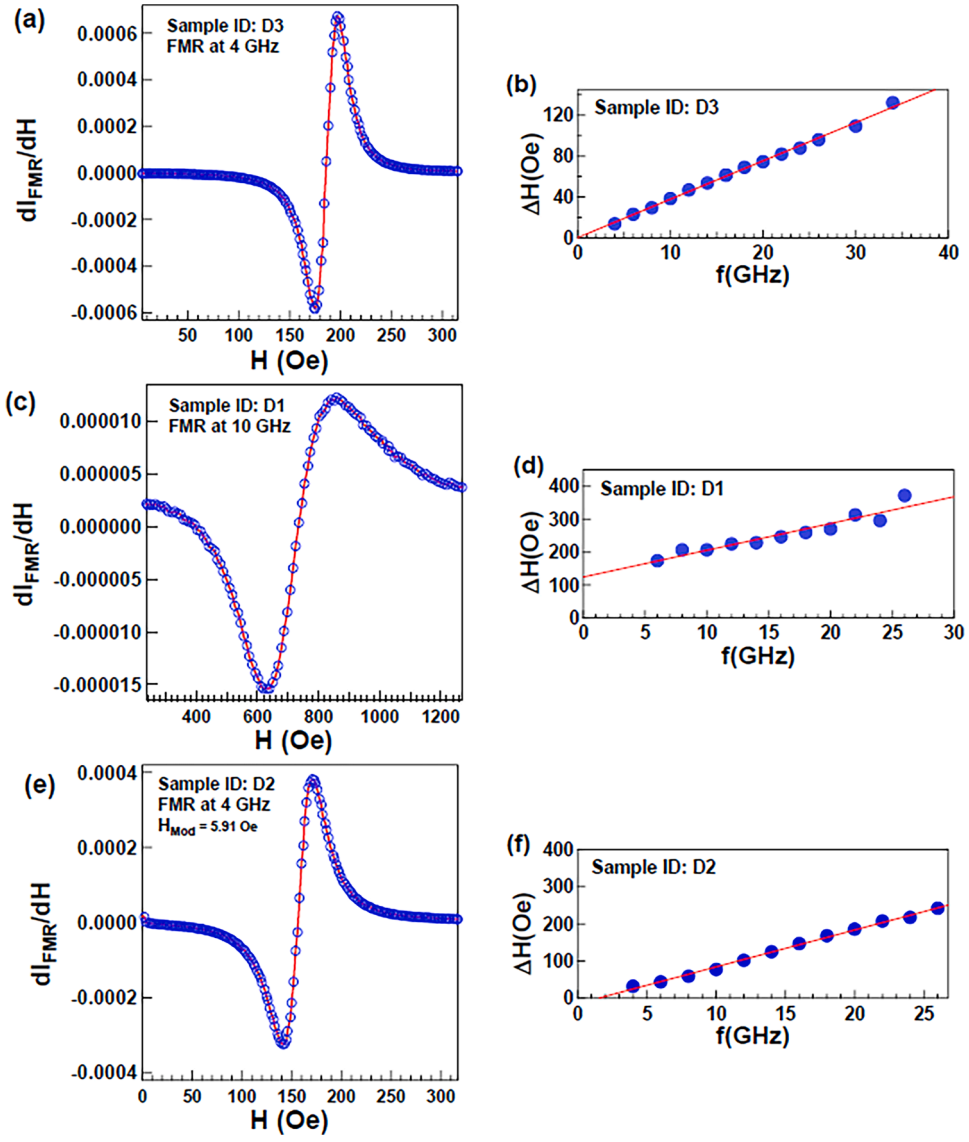

Fig. 7. (a, c, e) Examples of FMR traces for Samples D3, D1, and D2, respectively. (b, d, f) The FMR linewidth as a function of RF frequency for Samples D3, D1, and D2, respectively. From the linear fits, we extract the effective damping $\alpha_{eff} \sim 0.009$ for Sample D3, $\alpha_{eff} \sim 0.015$ for Sample D1, and $\alpha_{eff} \sim 0.024$ for Sample D2.

that the anisotropy followed a rough 100 Oe as shown previously [7] for low B content FeGaB, the M_{eff} does not change substantially although the error does lower ($M_{eff} = 1189 \pm 20$ Oe). Therefore, the difference between the effective and saturation magnetization of *D1* is likely due to a larger presence of perpendicular anisotropy energy present as $M_{eff} = M_{Sat} - \frac{2K}{M_{Sat}}$.

Figs. 7 (a,c,e) show our FMR measurements sorted based on the smallest α_{eff} to the largest value. Measurements are shown for samples *D3* and *D2* at 4 GHz, and 10 GHz for sample *D1*, where we can analyze the relationship between the FMR linewidth and FMR frequency. For sample *D1,* the FMR related to lower frequency (6 and 8 GHz), the spectrum has been provided in supporting information as Figure S5. The results are shown in Figs. 7 (b,d,f). Furthermore, we can extract an effective damping constant utilizing Eq. 2: [53,54]

$$\mu_0 \Delta H_{pp} = \mu_0 \Delta H_0 + \frac{2}{\sqrt{3}} \left(\frac{2\pi}{\gamma}\right) (\alpha_{eff} f) \quad (2)$$

where in Eq. 2, ΔH_{pp} is the FMR peak-to-peak linewidth extracted from the fit in Figs. 7 (a), (c) and (e), ΔH_0 is the zero-frequency linewidth, α_{eff} is the effective Gilbert damping constant, f is the RF frequency, and μ_0 is the permeability of free space. We utilize the extracted g-factors for samples *D1, D2*, and *D3* from their respective dispersion relationships for use in the gyromagnetic ratio, γ. From Eq. 2, we extract the effective Gilbert damping constant of sample *D3* to be $\alpha_{eff} \sim 0.009$. We utilize the term ***"effective damping constant"*** due to intrinsic and non-Gilbert extrinsic contributions to the FMR linewidth, such as two-magnon scattering. Although we do not observe nonlinearity associated with two-magnon scattering (Figs. 7 b,d,e), nonlinearity may still exist in a lower FMR frequency range <4 GHz, which we were not able to measure due to low FMR signal [55,56].

As shown in Figs. 7 (a-c), for samples *D1* and *D2*, similar FMR measurements were performed that allowed us to extract their effective damping constant of $\alpha_{eff} \sim 0.015$ and 0.024, respectively. We acknowledge some challenges involving fitting Eq. 1 as these fits are sensitive to the range of the fit and may be improved if higher and lower RF frequencies were possible for these samples. The nonphysical negative linewidth of *D2* at $f = 0$ (Figure 7 (f)) may be due to nonlinear effects that occur in lower RF frequencies, which we were not able to achieve due to large linewidth broadening and low FMR signal at lower frequencies and limitations of the instrument for higher frequencies, and that nonlinearity may be resultant of effects such as two-magnon scattering [55,56]. For *D2*, if we constrain the linewidth to be positive such that it is physical, the effective damping for *D2* does not change greatly and decreases to $\alpha_{eff} = 0.021$. *D2* and *D3* demonstrate a lower ΔH_0 (Figs. 7 (b,f)) by an order of magnitude than D1, and were deposited using longer sputtering times, double than that of *D1*. Thereby, longer sputtering times decrease the magnetic inhomogeneity, which agrees with previous results demonstrating lower magnetic inhomogeneity with higher boron doping content [7].

Time Resolved Magneto-Optical Kerr Effect

Circularly polarized pump pulses used in TR-MOKE can generate either spin polarization via optical orientation or through the opto-magnetic field because of the inverse Faraday effect, with both spin polarization directions parallel to the sample's normal [36]. In our TR-MOKE scheme (Fig. 1), the applied magnetic field (H) was perpendicular to the sample's surface, whereas the sample's magnetic easy axis (M) was in the plane (with saturation magnetization of ~1700 emu/cc below 100 Oe and a coercivity field of ~36 Oe, as shown in Fig. 3 (c), the black trace). We should note that our time-resolved setup did not allow us to apply the magnetic field in the plane of the sample, furthermore, similar measurements at RT also did not result in any observation of TR-MOKE.

In this study, when the probe light is reflected off a magnetized medium, the resulting rotation of the polarization plane of the light can provide information on the magnetization of the material. The photo-excited non-equilibrium spins can induce an instantaneous magnetic state and the relaxation of the spin population can be monitored through the rotation of a linearly polarized probe beam. In sample *D1*, the changes in the polarization of the reflected probe pulse ($\Delta\theta$) as a function of the time delay were mapped as a function of the magnetic field at 100 K.

We should also note the measurements presented in Figs. 8 (a,b) started from high fields, and then the field was ramped down to zero. This trend (starting from the highest field) was chosen to fully saturate the magnetization. We observed clear signatures of TR-MOKE from 10 to 0 Tesla and a systematic increase in the amplitude of Δθ. When the pump laser interacts with the magnetic film, ultrafast demagnetization occurs with energy transfer occurring between three energy baths: the spin, charge, and lattice subsystems [57]. We can use a phenomenological exponential fit to obtain information about our magnetization recovery times: [58,59]

$$\Delta\Theta_k(\Delta t) = \mathrm{erf}\left[2 \times \frac{t - t_0}{\tau_1}\right] \times \left[(A - B)e^{-\frac{t}{\tau_2}} + B\right] \quad (3)$$

Where in Eq. 3, $\Delta\Theta_k(\Delta t)$ is the change of Kerr angle as a function of the time delay between pump and probe, the error function is used as a cross-correlation function between the pump and probe, τ_1 is the initial fast recovery time capturing demagnetization and spin/electron recovery times, τ_2 is the long recovery time representing thermalization time of the lattice, and A/B is the total change of Kerr angle at the time of demagnetization ($0 < t < 2$ ps) and at the time where the Kerr angle has recovered to a steady value. The results are summarized in Table 3, and the fits using Eq. 3 are added to the TR-MOKE traces in Figs. 8 (a,b).

While τ_1 remains relatively stable with the applied field when accounting for their relatively large errors, which is most likely due to a lack of temporal resolution before 2 ps of delay time, τ_2 changes significantly with the field, even when considering their respective error ranges. There is a large change in the long magnetic recovery time (τ_2) when there is no applied field as compared to when a magnetic field is applied. Furthermore, it is of note that the initial magnetization never seems to recover at 0 T when sample *D1* is excited with circularly polarized light, instead reaching a new stable magnetization after 13.5 ps (τ_2). There is no change in magnetization when completing the same measurement at 2 T with linearly polarized light (Fig. 8 c), indicating a change in magnetization induced by a direct helicity-dependent magneto-optic interaction instead of a purely thermal interaction.

Probing the transient reflectivity also did not show any response at different magnetic fields, as shown in Fig. 8 (d). This helicity-dependent change of magnetization without an external magnetic field suggests the use of these soft FeGaB films for all-optical helicity-dependent switching. Applying an external magnetic field greatly increases the long τ_2 magnetic recovery time as the applied external field may help to reorient the optically changed magnetization of FeGaB to its initial magnetization, as previously seen in Co/Pt thin film multilayers [60]. Increasing the applied magnetic field increases the recovery time to a stable magnetization post-optical excitation, peaking at 6 T. Notably, at 10 T, there is very little change in total Kerr angle near 0 ps, indicating that this large magnetic field provides enough energy to prevent large ultrafast demagnetization caused by the pump. Temperature may also be a factor for our long recovery time of initial magnetization as our low temperature of 100 K may slow down recovery time. This lower temperature may also help with all optical helicity-dependent switching as opposed to higher ambient temperatures, in which recovery dynamics are more efficient [60]. Further work in MOKE microscopy can help reveal if the observed effect is truly an all-optical switching event or simply a very long recovery time above several hundred ps without any observed precession of magnetization. Furthermore, it has been shown

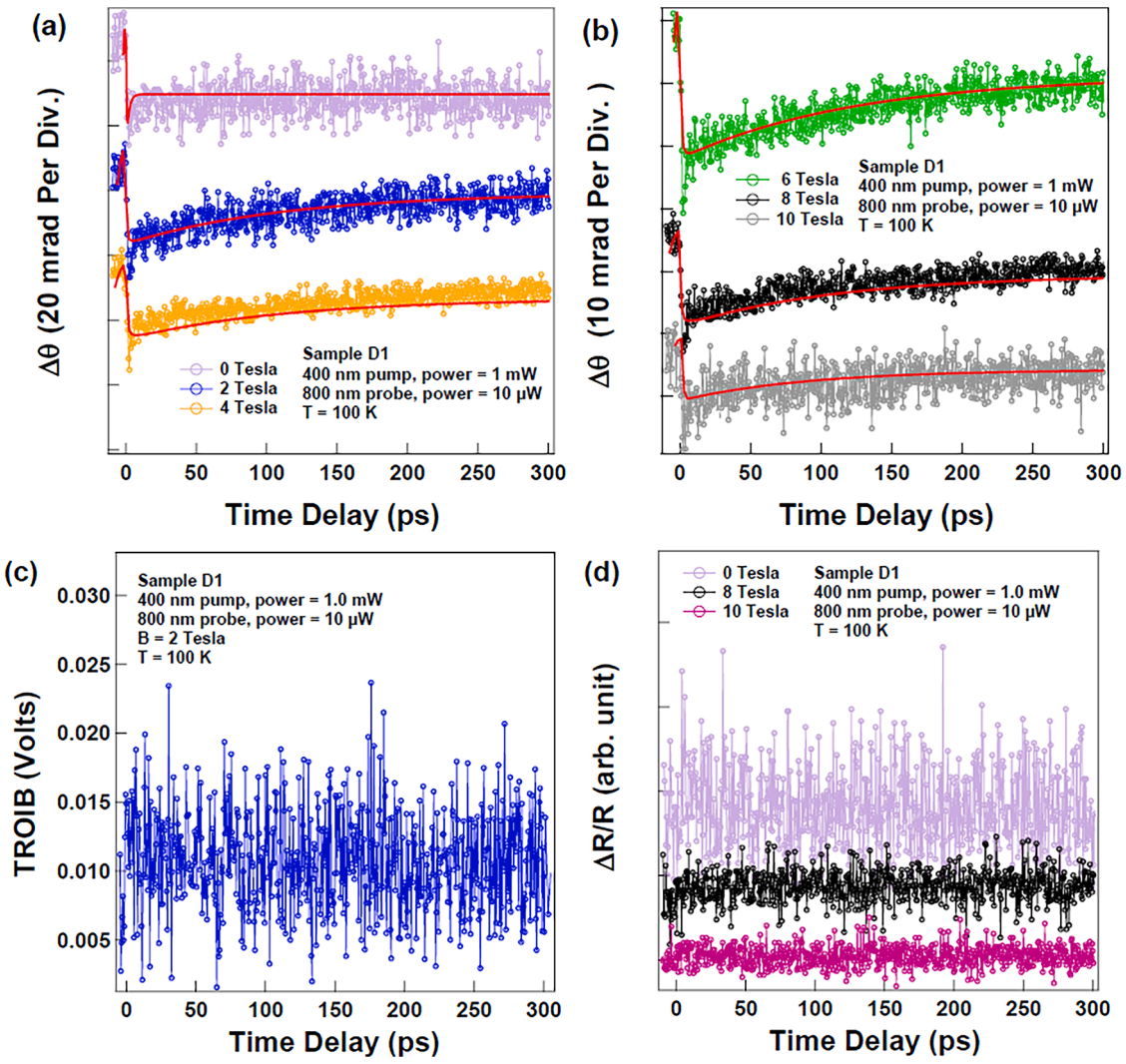

Fig. 8. (a,b) TRMOKE at 100 K of sample D1 at different magnetic fields. The amplitude of Δθ increased when the field was ramped down from 10 Tesla. The initial recovery of Δθ occurred in 10 ps, but the magnetization states did not fully recover in the time scale of 300 ps. The fits using Eq. 3 are added to the observed dynamics, and the extracted parameters are summarized in Table 3. (c) The Pump/probe response at 2 Tesla for sample D1 where both pulses were linearly polarized. We refer to this measurement as time-resolved optically induced birefringence (TROIB). (d) Time-resolved transient reflectivity at different magnetic fields for sample D1. The traces are shifted for clarity in the panels (a, b, c). We did not observe any variation in the measured dynamics. We should note that preliminary measurements did not show the precession of the ferromagnetic states when the field was applied to the plane.

Table 3
The extracted relaxation times employing Eq. 3 and the experimental data presented in Figs. 8 (a,b).

External Field (Tesla)	τ_1 (ps)	τ_2 (ps)
0	1.55 ± 0.863	13.50 ± 1.87
2	0.63 ± 0.36	85.74 ± 11.20
4	1.92 ± 0.42	96.10 ± 10.40
6	1.27 ± 0.27	100.74 ± 8.63
8	1.28 ± 0.33	80.54±7.82
10	0.98 ± 0.75	79.08±20.3

that longer recovery times of magnetization may be from increased spin-phonon recovery times. In CoFeB/MgO/CoFeB tunneling junctions, it has been shown that low exchange stiffness in relation to low Gilbert damping increases spin-phonon recovery time to be on the order of a few tens of ps, similar in time to our τ_2 value for our 0 T measurement. Therefore, our demonstrated long recovery time in our TR-MOKE observation is indicative of low exchange stiffness; however, further study, including careful modelling, is needed to better understand this connection [59].

Summary

In summary, we investigated the influence of sputtering conditions on the magnetic properties of FeGaB thin films grown by co-sputtering of FeGa and B targets. Structural and compositional characterization verified that increasing the B content reduces the grain size and amorphized the FeGaB film. We identified an optimal sputtering power combination (i.e., 60 W for FeGa, 40 W for B) to attain FeGaB films with soft magnetism and low effective damping. Additionally, employing a growth temperature of 200°C resulted in a low coercive field of ~6 Oe and an effective damping parameter of ~0.009, while retaining a saturation magnetization of ~770 emu/cc. Using time-resolved MOKE, we report for the first time the ultrafast magnetization dynamics in FeGaB films, indicating potential for all-optical magnetic memory due to long recovery times. These findings not only deepen our understanding of magnetization behavior in FeGaB systems but also present valuable insights for advancing applications including spintronics, magnetoelectrics, and high-speed data storage technologies.

CRediT authorship contribution statement

Sumanta Kumar Karan: Writing – review & editing, Writing – original draft, Visualization, Validation, Methodology, Investigation, Formal analysis, Data curation, Conceptualization. **Shweta Sharma:** Writing – review & editing, Writing – original draft, Visualization, Validation, Methodology, Investigation, Data curation, Conceptualization. **Nicholas W.G. Smith:** Writing – review & editing, Writing – original draft, Validation, Investigation. **Yannick Pleimling:** Writing – review & editing. **Stephen McGill:** Writing – review & editing. **Brenden A. Magill:** Writing – review & editing. **Shashank Priya:** Writing – review & editing, Supervision, Resources, Funding acquisition, Conceptualization. **Bed Poudel:** Writing – review & editing, Funding acquisition. **Giti A. Khodaparast:** Writing – review & editing, Writing – original draft, Validation, Supervision, Resources, Investigation, Funding acquisition.

Declaration of competing interest

The authors declare that they have no known competing financial interests or personal relationships that could have appeared to influence the work reported in this paper.

Acknowledgments

S. K. K. and S. S. conceived the idea. S.K.K and S. P acknowledges the support from NSF through grant number EECS-1904811, Army RIF program (W911W6-19-C-0083), ONR: N00014-21-1-2539 and ONR: N00014-22-1-2691. B.P. acknowledges the support through NSF I/UCRC: Center for Energy Harvesting Materials and Systems (CEHMS) and ONR: N00014-22-1-2691. G. A. K acknowledges partial support from AFOSR (Fund: FA9550-24-1-0059) and L. C. Hassinger Fellowship. We also acknowledge the support of Rachel Maizel in Prof. Satoru Emori's group at Virginia Tech for the help with the FMR measurements. A portion of this work was performed at the National High Magnetic Field Laboratory, which is supported by National Science Foundation Cooperative Agreements DMR-1644779 and DMR-2128556, and the State of Florida.

Supplementary materials

Supplementary material associated with this article can be found, in the online version, at doi:10.1016/j.mtelec.2026.100198.

Data availability

Data will be made available on request.

References

[1] C.R. Rementer, Tuning Magnetic Properties of Soft Ferromagnetic Thin Films for High Frequency Applications, University of California, Los Angeles, 2017.
[2] W. Yang, et al., Materials. (Basel) 15 (20) (2022) 7191.
[3] C. Wang, et al., Appl. Phys. Lett. 112 (19) (2018) 192401.
[4] K. Chopra, Thin film device applications, Springer Science & Business Media, 2012.
[5] I. Fergen, et al., J. Magn. Magn. Mater. 242 (2002) 146.
[6] M. Takahashi, et al., IEEE Trans Magn 26 (5) (1990) 1503.
[7] J. Lou, et al., Appl. Phys. Lett. 91 (18) (2007) 182504.
[8] A. Ludwig, E. Quandt, J. Appl. Phys. 87 (9) (2000) 4691.
[9] A. Acosta, et al., J. Appl. Phys. 128 (1) (2020) 013903.
[10] D. Cao, et al., AIP. Adv. 7 (11) (2017) 115009.
[11] E.d.T. De Lacheisserie, J. Peuzin, J. Magn. Magn. Mater. 136 (1-2) (1994) 189.
[12] R. Messier, MRS Bulletin 13 (11) (1988) 18.
[13] C.R. Rementer, et al., Appl. Phys. Lett. 110 (24) (2017) 242403.
[14] A.E. Clark, et al., IEEE Trans Magn 36 (5) (2002) 3238.
[15] L. Cabral, et al., ACS. Appl. Mater. Interfaces. 11 (1) (2018) 1529.
[16] P. Bartolomé, et al., The Journal of Physical Chemistry C 124 (8) (2020) 4717.
[17] C. Tu, et al., Materials. (Basel) 12 (14) (2019) 2259.
[18] D. Cao, et al., Applied Physics A 126 (9) (2020) 676.
[19] C. Wang, et al., Magnetochemistry. 8 (10) (2022) 111.
[20] M. Huang, et al., J. Appl. Phys. (7) (2008) 103.
[21] Q. Lin, et al., Nanomaterials 13 (22) (2023) 2948.
[22] G. Ramírez, et al., J. Magn. Magn. Mater. 535 (2021) 168047.
[23] L.R. Shah, et al., J. Appl. Phys. (9) (2010) 107.
[24] C. Dong, et al., Appl. Phys. Lett. (26) (2018) 113.
[25] X. Wu, et al., Appl. Phys. Lett. (16) (1995) 67.
[26] K. Yadagiri, et al., Journal of Materials Science: Materials in Electronics 33 (19) (2022) 15927.
[27] Y. Wang, et al., AIP. Adv. 12 (3) (2022) 035027.
[28] S. Imran, et al., Rare Metal Materials and Engineering 47 (7) (2018) 1951.
[29] M. Li, et al., Appl. Phys. Lett. (14) (2017) 110.
[30] M. Liu, et al., Advanced Materials 25 (10) (2013) 1435.
[31] M. Deb, et al., Appl. Phys. Lett. (25) (2015) 107.
[32] J. Wang, et al., Journal of Physics: Condensed Matter 18 (31) (2006) R501.
[33] M. Frazier, et al., Appl. Phys. Lett. (6) (2008) 92.
[34] K. Nontapot, et al., Appl. Phys. Lett. (14) (2007) 90.
[35] C.D. Stanciu, et al., Phys. Rev. Lett. 99 (4) (2007) 047601.
[36] G.-M. Choi, et al., Nat. Commun. 8 (1) (2017) 15085.
[37] C.-H. Lambert, et al., Science 345 (6202) (2014) 1337.
[38] K.T. Yamada, et al., Frontiers in Nanotechnology 4 (2022) 765848.
[39] A. Will-Cole, et al., Physical Review B 106 (17) (2022) 174401.
[40] V. Sharma, et al., Physical Review Materials 5 (12) (2021) 124410.
[41] D. Kuntu, et al., J. Magn. Magn. Mater. (2025) 173622.
[42] V. Mote, et al., Journal of theoretical and applied physics 6 (2012) 1.
[43] B. Cullity, et al., New Jersey (2001).
[44] H.P. Klug, John Wiley 1 (9–3) (1974) 687.
[45] S. Hassanzadeh-Tabrizi, J. Alloys. Compd. 968 (2023) 171914.
[46] Y. Zhang, et al., Phys. Metals Metall. 120 (2019) 626.
[47] Z. Wang, et al., Coatings 10 (4) (2020) 383.
[48] K. Yadagiri, et al., J. Mater. Sci. 33 (7) (2022) 3870.
[49] K. Yadagiri, et al., J. Mater. Sci. 58 (27) (2023) 11327.
[50] B. Arun, et al., Effect of RF power on magnetic properties and composition of FeGaB thin films, in: AIP Conference Proceedings, 2995, AIP Publishing LLC, 2024 020177.
[51] C. Kittel, Phys. Rev. 73 (2) (1948) 155.
[52] P. Bajracharya, et al., J. Phys. D. Appl. Phys. 55 (7) (2021) 075303.
[53] C.K. Mewes, T. Mewes, Handbook of Nanomagnetism: Applications and Tools (2015) 71.
[54] D.A. Smith, et al., Phys. Rev. Appl. 14 (3) (2020) 034042.
[55] R.D. McMichael, P. Krivosik, IEEE Trans Magn 40 (1) (2004) 2.
[56] S. Wu, et al., Physical Review B 105 (17) (2022) 174408.
[57] A. Kirilyuk, et al., Rev. Mod. Phys. 82 (3) (2010) 2731.
[58] J. Besbas, et al., Appl. Phys. Lett. (23) (2016) 108.
[59] B. Ji, et al., Appl. Phys. Lett. (11) (2023) 122.
[60] U. Parlak, et al., Physical Review B 98 (21) (2018) 214443.